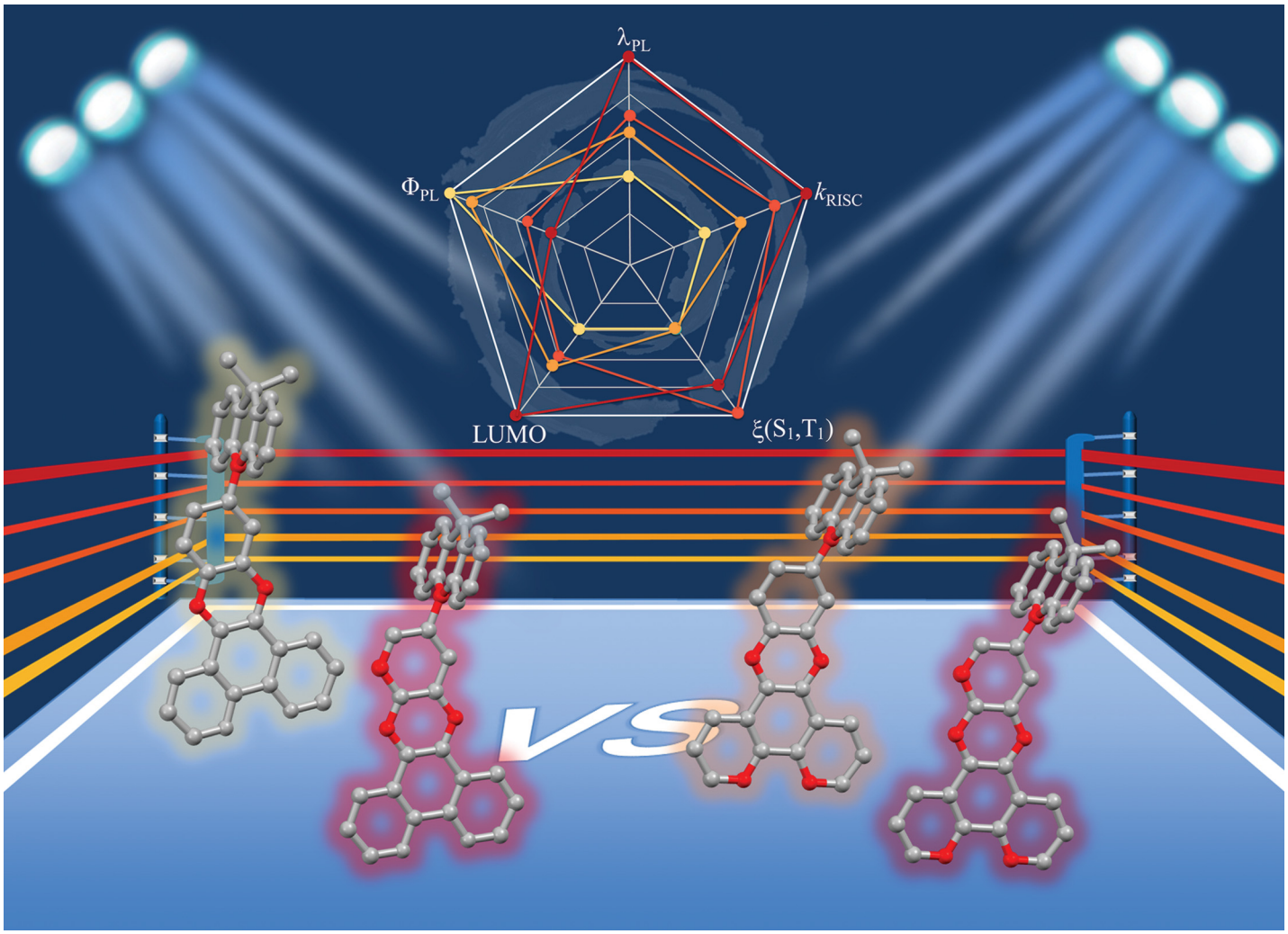

Highlighting research from the Zysman-Colman Group, Organic Semiconductor Centre, EaStCHEM School of Chemistry, University of St Andrews, UK

The influence of nitrogen doping of the acceptor in orange-red thermally activated delayed fluorescence emitters and OLEDs

A family of four orange-to-red TADF compounds containing different numbers of nitrogen atoms within the conjugated acceptor core has been systematically investigated. The findings indicate that increasing the nitrogen atom content in the acceptor of the D–A compounds results in a more stabilized LUMO, smaller ΔE_{ST} and faster k_{RISC}.

As featured in:

See Xiao-Hong Zhang, Eli Zysman-Colman *et al.*, *J. Mater. Chem. C*, 2023, **11**, 12174.

ROYAL SOCIETY OF CHEMISTRY

rsc.li/materials-c

Registered charity number: 207890

Journal of Materials Chemistry C

ROYAL SOCIETY OF CHEMISTRY

PAPER

View Article Online
View Journal | View Issue

Cite this: J. Mater. Chem. C, 2023, 11, 12174

The influence of nitrogen doping of the acceptor in orange-red thermally activated delayed fluorescence emitters and OLEDs†‡

Changfeng Si, §[a] Ya-Nan Hu, §[b] Dianming Sun, [a] Kai Wang, [b] Xiao-Hong Zhang *[bc] and Eli Zysman-Colman *[a]

Received 4th July 2023,
Accepted 18th August 2023

DOI: 10.1039/d3tc02352d

rsc.li/materials-c

Nitrogen-containing polycyclic aromatic hydrocarbons (N-PAH) have been widely used as deep lowest unoccupied molecular orbital (LUMO) acceptors in donor–acceptor (D–A) red thermally activated delayed fluorescence (TADF) emitters and in organic light-emitting diodes (OLEDs). However, most of the studies have focused disparately on donor/acceptor combinations to yield efficient emitters, while a methodological study investigating the influence of nitrogen (N) doping ratios on the ground and excited states of PAH acceptors is rare. Here, we report a family of four different N-PAH acceptors containing different numbers of nitrogen atoms within the N-PAH and their use in D–A TADF emitters, **DMACBP**, **DMACPyBP**, **DMACBPN** and **DMACPyBPN**, when coupled to the same donor, 9,9-dimethyl-9,10-dihydroacridine (DMAC). As the nitrogen content in the acceptor increases the LUMO becomes progressively more stabilized while the singlet–triplet energy gap (ΔE_{ST}) decreases and the rate constant for reverse intersystem crossing (k_{RISC}) increases. In particular, introducing nitrogen at the 10-position of dibenzo[*a*,*c*]phenazine (BP) leads to a more than ten-fold enhancement in k_{RISC} in **DMACPyBP** and **DMACPyBPN** compared to **DMACBP** and **DMACBPN**. Among the OLEDs with all four emitters that with **DMACBPN** demonstrates the highest EQE_{max} of 19.4% at an emission peak of 588 nm, while the deepest red emitting device employed **DMACPyBPN** (λ_{EL} = 640 nm) with an EQE_{max} of 5.4%.

Introduction

Thermally activated delayed fluorescence (TADF) is a photophysical mechanism that manifests itself in dual emission, a rapid prompt fluorescence from singlet excitons that decay radiatively, and a slow delayed fluorescence that occurs as a result of the thermal up-conversion of triplet excitons into singlets *via* reverse intersystem crossing (RISC) prior to light generation.[1–3] The efficient harvesting of both singlet and triplet excitons to produce light emission makes TADF materials particularly attractive as emitters for electroluminescent devices as, like phosphorescent devices, they can achieve 100% internal quantum efficiency (IQE).[4,5] Most of the reported TADF emitters employ a strongly twisted donor (D) and acceptor (A) structure, which leads to localization of the highest occupied molecular orbital (HOMO) and the lowest unoccupied molecular orbital (LUMO) on the D and A, respectively, and thus to a small singlet–triplet energy gap (ΔE_{ST}). A sufficiently small ΔE_{ST} is necessary to enable endothermic upconversion of triplet excitons to singlets by RISC.[6–8] The apparent paradox in TADF emitter design is that the design requirements for efficient RISC are in contrast to those to attain high photoluminescence quantum yield (Φ_{PL}), which require significant orbital overlap to maximize the oscillator strength of the transition.[9,10] Balancing these two criteria in the design of high-performance orange-red emitters becomes that much more difficult as radiative decay decreases while non-radiative decay increases due to the energy-gap law.[11–13] The general molecular design principles for red/deep red D–A TADF emitters are: (1) use of strong donor and acceptor motifs is a common strategy, affording a shallow HOMO and a deep LUMO for D and A, respectively; and (2) construction of a rigid and typically planar fused ring donor and/or acceptor for the suppression of nonradiative transitions. Within this model, most of the acceptors are

[a] Organic Semiconductor Centre, EaStCHEM School of Chemistry, University of St Andrews, St Andrews KY16 9ST, UK. E-mail: eli.zysman-colman@st-andrews.ac.uk
[b] Institute of Functional Nano & Soft Materials (FUNSOM), Joint International Research Laboratory of Carbon-Based Functional Materials and Devices, Soochow University, Suzhou, Jiangsu 215123, P. R. China. E-mail: xiaohong_zhang@suda.edu.cn
[c] Jiangsu Key Laboratory of Advanced Negative Carbon Technologies, Soochow University, Suzhou, 215123, Jiangsu, P. R. China

† The research data supporting this publication can be accessed at https://doi.org/10.17630/ccda8f8c-932f-498a-83e5-a2f95bcebf85

‡ Electronic supplementary information (ESI) available: ^{1}H and ^{13}C NMR spectra, HRMS and EA of all target compounds; supplementary computational data; supplementary photophysical data. See DOI: https://doi.org/10.1039/d3tc02352d

§ Equal contribution.

derivatives of either acenaphtho[1,2-*b*]pyrazine-8,9-dicarbonitrile (APDC),[14] heterocyclic quinoxaline-6,7-dicarbonitrile (QCN),[15] 11,12-dicyanodibenzo[*a*,*c*]phenazine (CNBPz),[16] 2,3-dicyanodibenzo[*f*,*h*]quinoxaline (CNBQx),[17,18] or dibenzo[*a*,*c*]-phenazine-3,6-dicarbonitrile (PZCN).[19] Nitrogen-doped polycyclic aromatic hydrocarbons (N-PAH), like dibenzo[*a*,*c*]phenazine (BP), have proven to be particularly popular as moieties in orange-red TADF emitters (Fig. S1, ESI‡).[20–26] Zhao *et al.* first reported BP-based TADF compounds, containing one-to-three 9,9-dimethyl-9,10-dihydroacridine (DMAC) donor moieties (Fig. S1, ESI‡). The orange-red OLEDs with **3DMAC-BP**, an emitter with three DMAC donors situated at the 3-, 6-, and 11-positions of the BP, showed a maximum external quantum efficiency (EQE_{max}) of 22.0% with an electroluminescence peaking at λ_{EL} = 606 nm.[23] Yang *et al.* reported a related compound using the BP acceptor, **DMAC-11-DPPZ** with the DMAC donor attached at the 11-position of the BP acceptor, which emits at λ_{PL} of 576 nm, has a photoluminescence quantum yield, Φ_{PL}, of 57% and a delayed lifetime, τ_d, of 1.53 μs in 10 wt% doped films in CBP. The optimized OLED with **DMAC-11-DPPZ** displays an orange emission at 588 nm with an EQE_{max} of 23.8%.[24] Tang *et al.* introduced one more nitrogen at the 10-position of the BP core to generate a new acceptor unit, BPQ. Star-shaped isomers **3,6,11-triAC-BPQ** and **3,6,12-triAC-BPQ** contain three DMAC donors at either the 3,6,11-positions or 3,6,12-positions of BPQ. **3,6,12-triAC-BPQ** showed a small red-shifted emission at 611 nm in toluene and a slightly shorter τ_d of 2.25 μs in 15 wt% doped films in mCBP compared to **3DMAC-BP** (λ_{PL} = 605 nm in toluene, τ_d = 2.9 μs in 20 wt% doped films in mCBP), which is a compound that does not have an N-atom at the 10-position of the acceptor. In contrast, **3,6,11-triAC-BPQ** exhibited a blue-shifted emission at λ_{PL} of 565 nm compared to **3,6,12-triAC-BPQ**. The devices with **3,6,11-triAC-BPQ** and **3,6,12-triAC-BPQ** showed an EQE_{max} of 22.0% [λ_{EL} = 581 nm, Commission International de l'Éclairage, CIE, coordinates of (0.51,0.48)] and 16.5% [λ_{EL} = 616 nm, CIE coordinates of (0.58,0.39)], respectively.[25] The same group reported an orange-yellow TADF material **DPPZ-DMAC**, where the related DPPZ acceptor contains two additional nitrogen atoms compared to BP. This compound emits at ~590 nm, has a smaller ΔE_{ST} of 0.01 eV, and a higher Φ_{PL} of 91.6% in 6 wt% doped films in CBP, compared to that of **DMAC-11-DPPZ**, a compound without the two additional nitrogen atoms in the acceptor. The **DPPZ-DMAC**-based device showed an EQE_{max} of 27.8% with λ_{EL} at 598 nm. Zhang *et al.* reported a similar emitter **SAF-2NP** that employs a structurally related 10*H*-spiro-(acridine-9,9′-fluorene) (SAF) donor instead of DMAC in combination with the same acceptor as **DPPZ-DMAC**. As excepted, **SAF-2NP** shows similar photophysics as **DPPZ-DMAC** but has a slightly blue-shifted emission at l_{PL} of ~580 nm and a much higher Φ_{PL} of 99%. The **SAF-2NP**-based OLED demonstrated a very high EQE_{max} of 32.5% with an λ_{EL} at 576 nm, an efficiency linked to the high Φ_{PL} of 99% and horizontally oriented transition dipole ($\Theta_{\parallel}$) of 85% of the emitter in the host matrix. When DPPZ is coupled with a triphenylamine (TPA) donor, as in **oTPA-DPPZ**, the emission shifts to the red at 605 nm in the 30 wt% doped films (Φ_{PL} = 75%; ΔE_{ST} of 0.07 eV).[26] The OLEDs with **oTPA-DPPZ** showed an EQE_{max} of 18.5% at λ_{EL} of 600 nm. By adjusting the position of the TPA groups, a "T-shape" deep-red TADF emitter, **pTPA-DPPZ**, was obtained.[26] Compared to **oTPA-DPPZ**, the rational spatial arrangement of D and A groups in **pTPA-DPPZ** accelerated radiative decay from the singlet state by 90-fold, giving rise to a Φ_{PL} of 87% in the neat film. The corresponding OLEDs, having a simplified bilayer non-doped structure, showed an EQE_{max} of 12.3% at λ_{EL} of 652 nm.

Examples of D–A TADF emitters have illustrated that the use of N-PAHs like BP or DPPZ accesses orange-to-red emission. Although numerous molecules have been reported, to the best of our knowledge, there is no one study that has been conducted to correlate the number of nitrogen atoms in the N-PAH acceptor (Fig. 1(a)) to the photophysical properties of the emitter. To address this question, we designed and synthesized four DMAC-containing TADF emitters containing different numbers of nitrogen atoms in the N-PAH acceptor: 11-(9,9-dimethylacridin-10(9*H*)-yl)dibenzo[*a*,*c*]phenazine (**DMACBP**) (2 nitrogen atoms), 12-(9,9-dimethylacridin-10(9*H*)-yl)dibenzo[*f*,*h*]-pyrido[2,3-*b*]quinoxaline (**DMACPyBP**) (3 nitrogen atoms), 11-(9,9-dimethylacridin-10(9*H*)-yl)dipyrido[3,2-*a*:2′,3′-*c*]phenazine (**DMACBPN**) (4 nitrogen atoms) and 12-(9,9-dimethylacridin-10(9*H*)-yl)pyrido[2′,3′:5,6]pyrazino[2,3-*f*][1,10]phenanthroline (**DMACPyBPN**) (5 nitrogen atoms). The variations in key photophysical properties of these four emitters are summarized in Fig. 1(b). It becomes clear that the rate of reverse intersystem crossing, k_{RISC}, can be enhanced when the BP acceptor is modified to contain an additional nitrogen atom at the 10-position. The OLEDs with **DMACBPN** demonstrated an EQE_{max} of 19.4% at λ_{EL} of 588 nm. The EL spectra shift to red when there is an increasing nitrogen content in the acceptor, with the reddest device using **DMACPyBPN** emitting at 640 nm.

Results and discussion

Synthesis and characterization

The synthesis of **DMACBP**, **DMACPyBP**, **DMACBPN** and **DMAC-PyBPN** is outlined in Scheme 1. The intermediates **DMACPhSN** and **DMACPySN** were obtained by a nucleophilic substitution reaction between 5-fluorobenzo[*c*][1,2,5]thiadiazole and 9,9-dimethyl-9,10-dihydroacridine (DMAC), and Buchwald–Hartwig coupling between 6-bromo-[1,2,5]thiadiazolo[3,4-*b*]pyridine and DMAC, respectively, followed by ring-opening of the benzothiadiazole (BTD) with lithium aluminum hydride ($LiAlH_4$). Intermediate **1** was then reacted with phenanthrene-9,10-dione and 1,10-phenanthroline-5,6-dione in 1-butanol to afford **DMACBP** and **DMACBPN**, respectively, in good yield. **DMACPyBP** and **DMACPyBPN** were obtained from the reaction of **2** with phenanthrene-9,10-dione and 1,10-phenanthroline-5,6-dione in 1-butanol, respectively. The structural identity and purity of the four emitters were verified by ^1H and ^{13}C nuclear magnetic resonance (NMR) spectroscopy, melting point determination, high-resolution mass spectrometry, elemental analysis, and high-performance liquid chromatography (HPLC) (Fig. S2–S24, ESI‡).

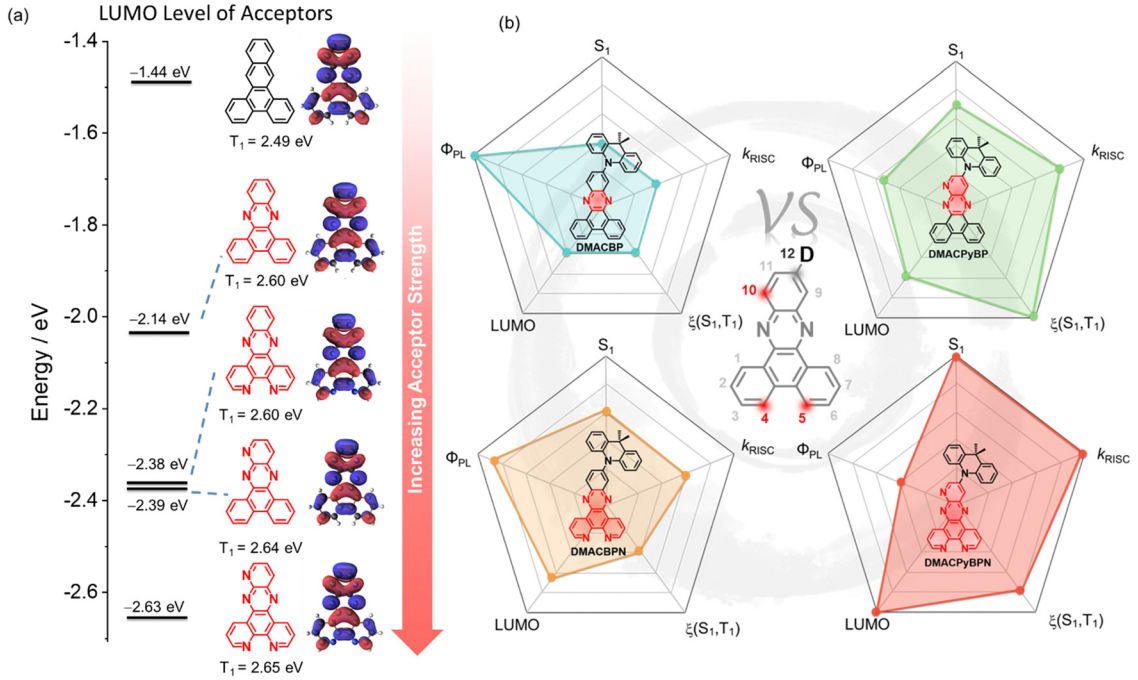

Fig. 1 (a) Electron-accepting capability (the LUMO level) of nitrogen-doped PAH acceptor units, estimated at the PBE0/6-31G(d,p) level. (b) The main parameters (Φ_{PL}, S_1, LUMO, k_{RISC}, and ξ (S_1, T_1)) values *vs.* four emitters with different N/C ratio acceptors in this work.

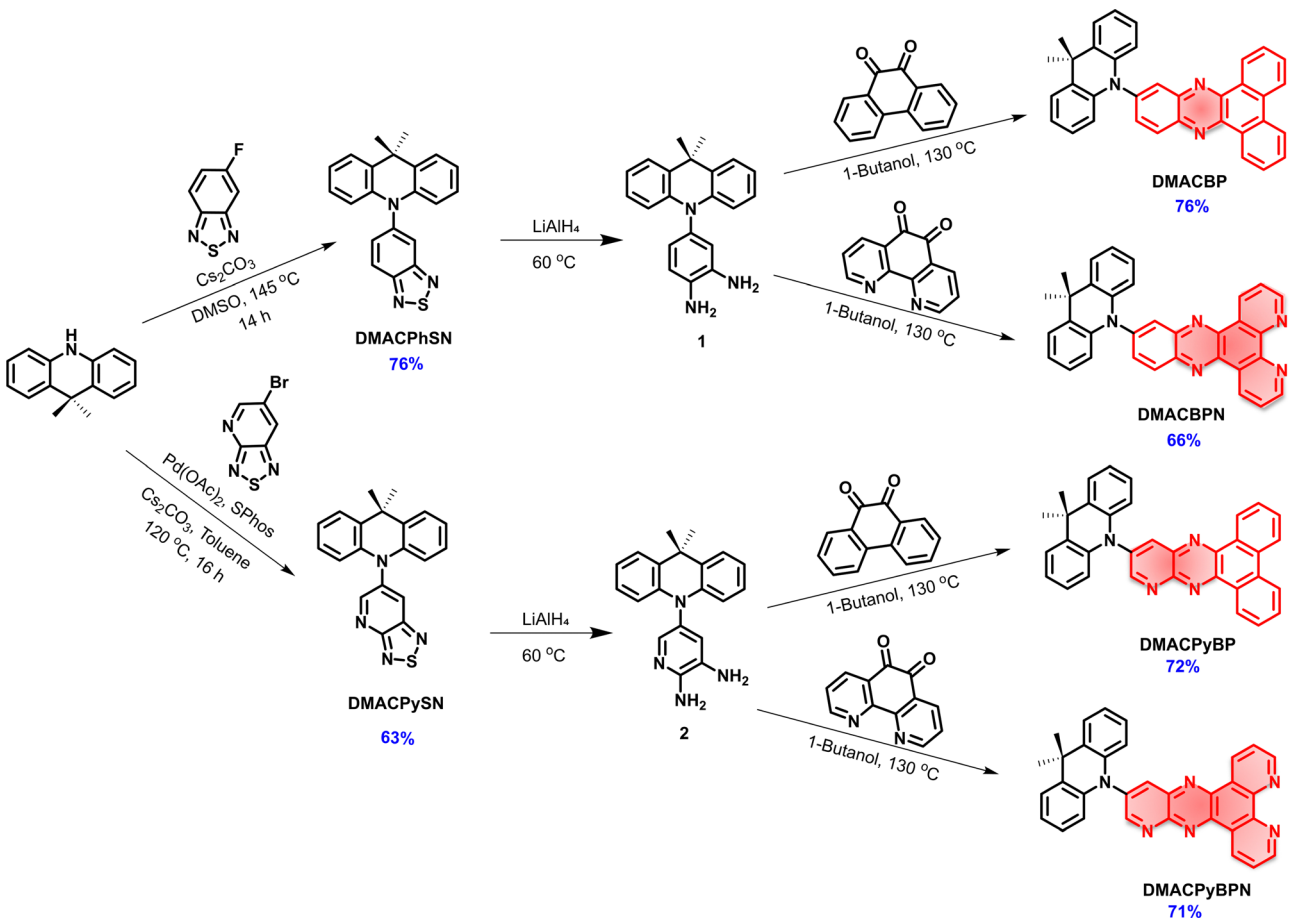

Scheme 1 Synthetic routes for **DMACBP**, **DMACPyBP**, **DMACBPN** and **DMACPyBPN** emitters.

To predict their optoelectronic properties, we first modelled the ground-state structure of the four emitters in the gas phase using density functional theory (DFT) at the PBE0/6-31G(d,p) level of theory (Fig. 2). The calculated energy levels of the highest occupied molecular orbital (HOMO) and the lowest unoccupied molecular orbital (LUMO) are shown in Fig. 2(a) and Fig. S25 (ESI‡). As expected, the HOMO is localized on the DMAC donor while the LUMO is localized on the nitrogen-rich electron acceptors. The gradually stabilized LUMO from **DMACBP** to **DMACPyBP**, **DMACBPN** and **DMACPyBPN** originates from the enhanced electron-withdrawing strength of the acceptor with increasing nitrogen content. However, due to the enhanced electronic coupling between the donor and the acceptor, the HOMO levels of **DMACPyBP** and **DMACPyBPN** are more stabilized as these are delocalized over both DMAC and the pyridine (Py) rings, as compared to the DMAC-localized orbitals in **DMACBP** and **DMACBPN** (Fig. 2(a)). The HOMO–LUMO gap, $\Delta E_{\mathrm{HOMO-LUMO}}$, decreases from 2.84 eV for **DMACBP**, to 2.75 eV for **DMACPyBP**, 2.72 eV for **DMACBPN** and 2.63 eV for **DMACPyBPN**, following a trend similar to that observed for the LUMO and governed by the strength of the electron-acceptor moiety.

The excited-state properties were then calculated using the time-dependent DFT (TD-DFT) within the Tamm–Dancoff approximation (TDA) based on the optimized ground-state geometry.[27] The S_1 energies are 2.17 eV for **DMACBP**, 2.04 eV for **DMACPyBP**, 2.05 eV for **DMACBPN** and 1.91 eV for **DMACPyBPN**, while the T_1 energies likewise decrease from 2.15 eV, to 2.00 eV, 2.03 eV and 1.89 eV, respectively, following a trend of increasingly stabilized excited states with increasing N atom content in the acceptor, although **DMACPyBP** and **DMACBPN** are close in energy. The corresponding ΔE_{ST} values are all relatively small at 0.02, 0.04, 0.02 and 0.03 eV, due to the large dihedral angles between the DMAC and the acceptor that effectively minimize the electronic coupling [**DMACBP** (82.2°), **DMACPyBP** (82.7°), **DMACBPN** (83.8°) and **DMACPyBPN** (86.1°) based on the optimized S_0 geometries] (Fig. S26, ESI‡). To gain insight into the photophysical properties of the S_1 excited states, we performed natural transition orbital (NTO) analyses at the S_0 geometry (Fig. 2(b)). The S_1 state of each of the compounds possesses an evident intramolecular charge transfer (ICT) character. Hole and electron distributions mirror HOMO/LUMO localization, respectively. Root-mean-square displacements (RMSDs) between S_0, S_1 and T_1 were calculated (Fig. 2(c) and Fig. S27, ESI‡) using the VMD program to evaluate the structural changes that occur upon excitation and intersystem crossing.[28] The RMSD values of **DMACBP**, **DMACPyBP**, **DMACBPN** and **DMACPyBPN** between S_0 and S_1 were simulated to be 0.17, 0.14, 0.13 and 0.07 Å, respectively. The smaller RMSD of **DMACPyBPN** indicates that the introduction of N at the 10-position or 4/5-position reduces the magnitude of structural relaxation. In the relaxed S_1 geometry, there is a larger S_1–T_1 spin–orbit coupling (SOC) matrix element of 0.05 cm^{-1} in **DMACPyBP** and of 0.04 cm^{-1} in **DMACPyBPN** than that in **DMACBP** (0.01 cm^{-1}) and **DMACBPN** (0.01 cm^{-1}) (Fig. 2(b)), indicating that the rate constants of intersystem crossing (k_{ISC}) in **DMACPyBP** and **DMACPyBPN** will be faster than in the latter two compounds. As shown in the electrostatic potential maps (Fig. S38, ESI‡), the nitrogen-rich components have a more negative electrostatic potential while the other parts have a neutral and a positive potential, which correlates with the trend in increasing electron-withdrawing ability of the acceptor with the inclusion of an increasing number of nitrogen atoms within the acceptor moiety.

Photophyiscal investigations

The energies of the frontier molecular orbitals (FMOs) were inferred from the electrochemical behavior of **DMACBP**, **DMACPyBP**, **DMACBPN** and **DMACPyBPN** by cyclic voltammetry (CV) and differential pulse voltammetry (DPV) in degassed dichloromethane (DCM) with tetra-*n*-butylammonium hexafluorophosphate ([^{n}Bu$_4$N]PF$_6$) as the supporting electrolyte (Fig. 3(a)). Electrochemical potentials are reported *versus* a saturated calomel electrode. The reduction potentials (E_{red}), determined from the DPV peak values, are −1.39 V (**DMACBP**), −1.22 V (**DMACPyBP**), −1.33 V (**DMACBPN**) and −1.11 V (**DMACPyBPN**), respectively, reflecting the expected anodic shift associated with increasing acceptor strength that is mirrored in the trend of the calculated LUMO levels from BP < BPN < PyBP < PyBPN (Fig. 1(a)). The calculated LUMO energies are –2.94 eV, −3.12 eV, −3.00 eV and −3.20 eV for **DMACBP**, **DMACPyBP**, **DMACBPN** and **DMACPyBPN**, respectively. **DMACPyBP** (1.04 V) and **DMACPyBPN** (1.04 V) have more positive oxidation potentials than those of **DMACBP** (1.00 V) and **DMACBPN** (0.98 V), in line with the DFT calculations. The HOMO levels of **DMACBP**, **DMACPyBP**, **DMACBPN** and **DMACPyBPN** are −5.34, −5.39, −5.33 and −5.39 eV, respectively. The HOMO–LUMO gaps for **DMACBP**, **DMACBPN** and **DMACPyBPN** are 2.40, 2.33 and 2.19 eV, respectively, which mirror the trend in the DFT calculated values of 2.84, 2.72, and 2.63 eV; however, **DMACPyBP** exhibits a much smaller HOMO–LUMO gap (2.27 V) inferred from its electrochemistry than **DMACBPN** (2.33 V), which is opposite to the DFT calculated results in the gas phase. However, the inferred LUMO energies obtained from CV exactly mirror the trend from the DFT calculated LUMO of the acceptors as shown in Fig. 1(a). The inconsistency of the data for **DMACPyBP** to its corresponding acceptor likely indicates a deviation of the D–A dihedral angles between the DFT calculated structure in the gas phase and that exists in solution during the CV acquisition.

The UV-Vis absorption spectra of the four emitters in dilute toluene are shown in Fig. 3(b). The spectra show two prominent spectral features, with two intense bands centered at ∼390 nm and a hypochromic broadband at ∼470 nm, which are assigned to locally excited (LE) π–π* transitions of the donor and acceptor moieties,[30,31] and intramolecular charge transfer (ICT) transitions of the DMAC donor to the acceptor moiety, respectively.[24,30] The ICT band expectedly shifts to lower energies with the introduction of an increasing number of N atoms at positions 4/5 of the acceptor; for instance, the ICT band at 465 nm of **DMACBPN** ($\varepsilon = 2.5 \times 10^3$ M^{-1} cm^{-1}) is red-shifted compared to that of **DMACBP** (λ_{abs} = 458 nm, $\varepsilon = 1.8 \times 10^3$ M^{-1} cm^{-1}) while those of **DMACPyBP** and **DMACPyBPN** absorb at essentially the same energy at 474 and 475 nm ($\varepsilon = 3.2 \times 10^3$ M^{-1} cm^{-1} for both), which match well with the

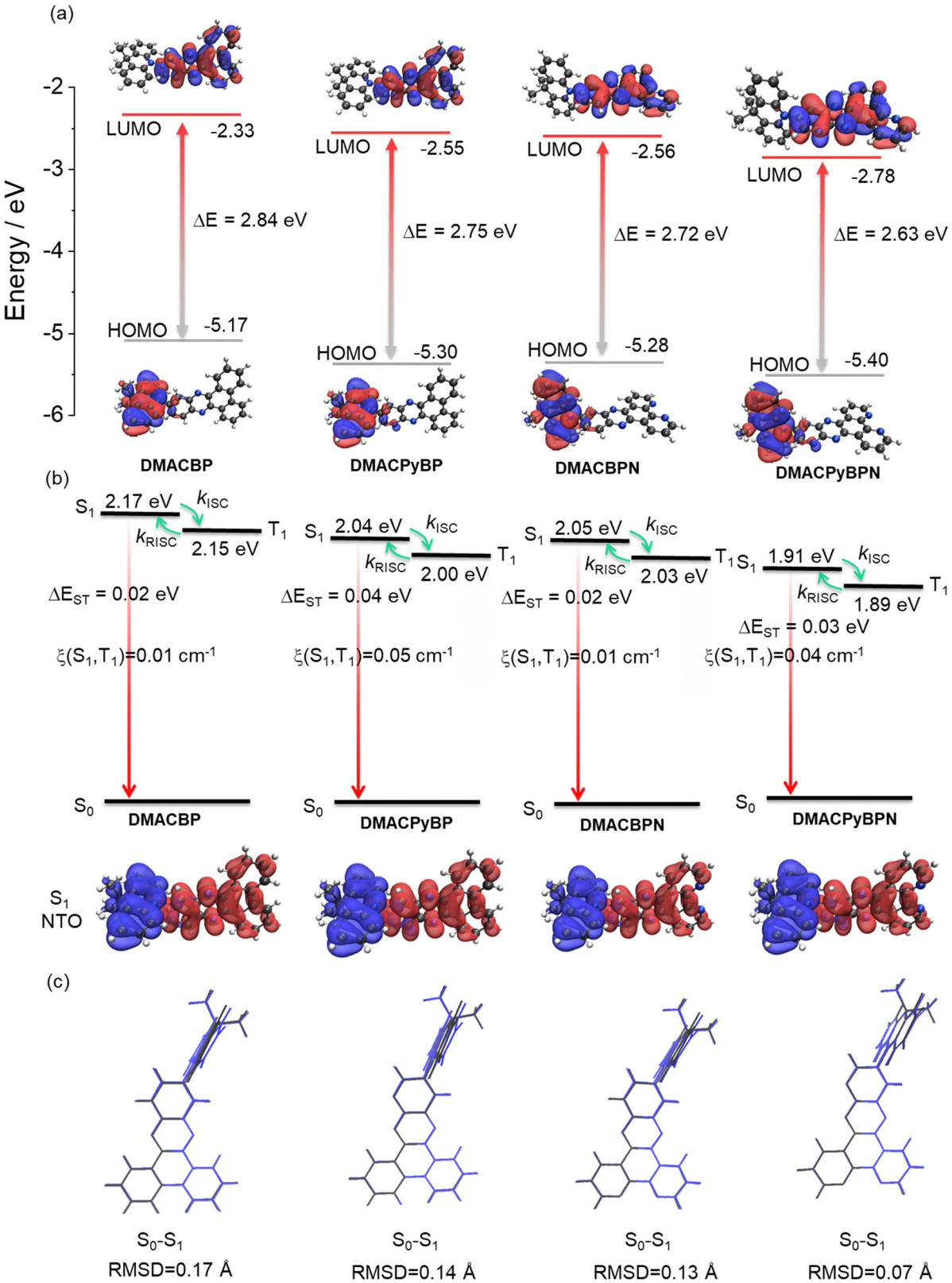

Fig. 2 (a) Frontier molecular orbitals (isovalue: 0.02) and (b) Vertical excitation energy levels, natural transition orbitals (unoccupied (hole, blue) & occupied (electron, red)), (isovalue: 0.02) of S_1 of **DMACBP**, **DMACPyBP**, **DMACBPN** and **DMACPyBPN** calculated at the optimized S_0 geometry in the gas phase at the PBE0/6-31G(d,p) level. (c) Comparison of optimized structures of **DMACBP**, **DMACPyBP**, **DMACBPN** and **DMACPyBPN** at S_0 (grey) and S_1 (blue) states.

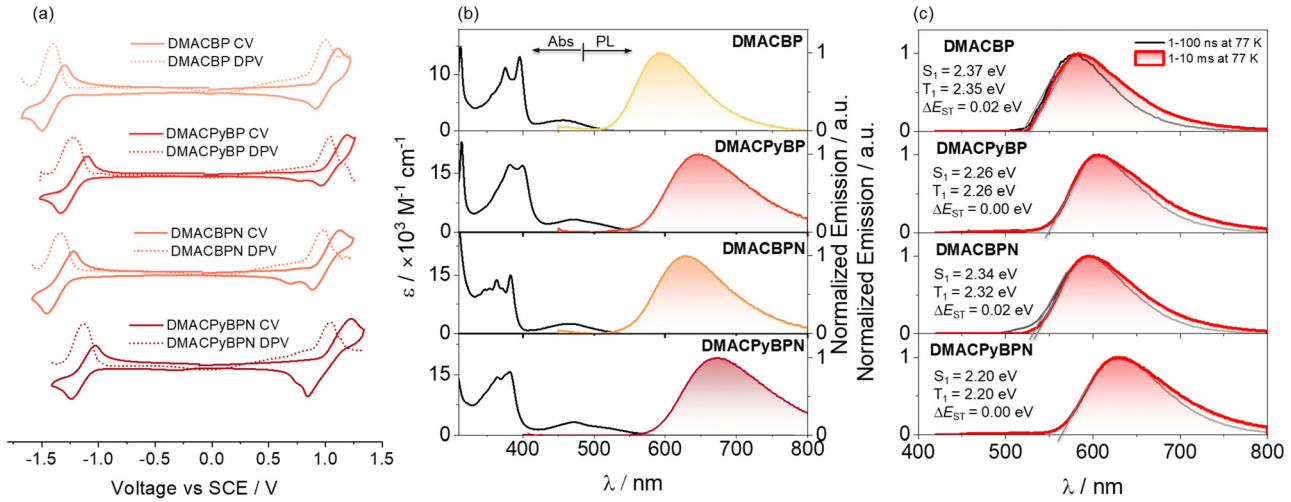

Fig. 3 (a) Cyclic and differential pulse voltammograms measured in degassed DCM with 0.1 M $[^nBu_4N]PF_6$ as the supporting electrolyte and Fc/Fc^+ as the internal reference (0.46 V *vs.* SCE).[29] Scan rate = 100 mV s^{-1}. (b) UV-vis absorption and steady-state photoluminescence (SSPL) spectra of **DMACBP**, **DMACPyBP**, **DMACBPN** and **DMACPyBPN** recorded in toluene at room temperature (λ_{exc} = 375 nm). (c) Prompt fluorescence (1–100 ns) and phosphorescence spectra (1–10 ms) in 2-MeTHF at 77 K of **DMACBP**, **DMACPyBP**, **DMACBPN** and **DMACPyBPN** (λ_{exc} = 375 nm).

TD-DFT calculated S_1 energies (Fig. 2(b)). Positive photoluminescence (PL) solvatochromism is observed for all compounds (Fig. S29 and Table S1, ESI‡), which is consistent with the ICT nature of the emissive excited state.

The steady-state photoluminescence (SSPL) spectra in toluene gradually red-shift from **DMACBP** (λ_{PL} = 595 nm) to **DMACBPN** (λ_{PL} = 630 nm) and **DMACPyBPN** (λ_{PL} = 672 nm), which coincides with an increasing number of nitrogen atoms in the acceptors (Fig. 3(b)). However, **DMACPyBP** (λ_{PL} = 645 nm) containing three nitrogen atoms within the acceptor exhibits a slightly red-shifted emission than **DMACBPN** (λ_{PL} = 630 nm), which contains four nitrogen atoms within the acceptor. This behavior correlates with the calculated S_1 energies (Fig. 2(b))and demonstrated that acceptor **PyBP** with 10-position N showed stronger electron-withdrawing abilities than **BPN** acceptor with two N in [1,10] phenanthroline, following the trend of acceptor strength as shown in Fig. 1(a). The corresponding optical band-gaps, determined from the intersection point of the normalized absorption and emission spectra,[32–34] for **DMACBP**, **DMACPyBP**, **DMACBPN** and **DMACPyBPN** are 2.37 eV, 2.20 eV, 2.31 eV and 2.12 eV, respectively (Fig. S30, ESI‡), which is consistent with the trend in emission energies (Fig. S31, ESI‡ and Table 1). The photoluminescence quantum yields (Φ_{PL}) for **DMACBP**, **DMACPyBP**, **DMACBPN** and **DMACPyBPN** in degassed toluene solution are 35%, 20%, 38% and 6%, respectively. When exposed to oxygen, these values significantly decrease to 9%, 7%, 8%, and 3% respectively. The energies of the onset of the prompt fluorescence and phosphorescence spectra in 2-MeTHF glass at 77 K were used to determine the S_1 and T_1 energies (Fig. 3(c)). The S_1 energies are 2.37, 2.26, 2.34 and 2.20 eV, while the T_1 energies are 2.35, 2.26, 2.32 and 2.20 eV, for **DMACBP**, **DMACPyBP**, **DMACBPN** and **DMACPyBPN**, respectively. As both the prompt fluorescence and phosphorescence spectra are structureless, it is reasonable to assign both the S_1 and T_1 states as possessing significant CT character. The corresponding ΔE_{ST} values for **DMACBP**, **DMACPyBP**, **DMACBPN** and **DMACPyBPN** are then 0.02 eV, 0.00 eV, 0.02 eV and 0.00 eV, respectively, which align with the TDA-DFT calculated results (Fig. 2(b)).

From the difference in transient PL decay behavior under aerated and degassed conditions in toluene, it is clear that the delayed emission is significantly quenched by the presence of oxygen (Fig. 4); interestingly, the quenching of the PL in

Table 1 Summary of photophysical properties of nitrogen-doped PAH acceptor-based compounds

Molecule	λ_{abs}/(ε/× 10^3 M^{-1} cm^{-1}) /nm[a]	λ_{PL}[a]/ nm	τ_p/ ns[a]	τ_d/ μs[a]	λ_{PL}[b]/ nm	Φ_{PL}[b]/ %	S_1/T_1[c]/ eV	ΔE_{ST}/ eV	τ_p/ ns[d]	τ_d/ μs[d]	k_{ISC}[e]/ $\times 10^7$ s^{-1}	k_{RISC}[e]/ $\times 10^4$ s^{-1}	E_{HOMO}[f]/ eV	E_{LUMO}[f]/ eV	E_g[g]/eV
DMACBP	395 (13), 458(1.8)	595	18	146	568	75(56)	2.33/2.31	0.02	15.3	130.3	1.7	1.0	−5.34	−2.94	2.40
DMACPyBP	400 (17), 474(3.2)	645	20	3.5	601	47(41)	2.32/2.31	0.01	21.1	5.9	0.6	19.4	−5.39	−3.12	2.27
DMACBPN	383 (15), 465(2.5)	630	27	19.7	586	71(52)	2.26/2.25	0.01	22.4	47.2	1.2	2.9	−5.33	−3.00	2.33
DMACPyBPN	382 (16), 475(3.2)	672	10	2.3	606	37(30)	2.32/2.31	0.01	23.2	2.9	0.8	42.6	−5.39	−3.20	2.19

[a] In PhMe at 298 K (λ_{exc} = 340 nm). [b] Spin-coated 2 wt% emitters doped in CBP films and Φ_{PL} values were determined using an integrating sphere (λ_{exc} = 340 nm). Values quoted are under N_2. Values in parentheses are in air. [c] S_1 was obtained from the onset of the prompt emission (time-gated window: 1–100 ns) ms measured in doped film at 77 K and T_1 was obtained from the onset of the phosphorescence spectrum (time-gated window: 1–10 ms) measured in doped film at 77 K. [d] PL lifetime. [e] k_{ISC} = intersystem crossing rate constant from S_1 to T_1 states; k_{RISC} = reverse intersystem crossing rate constant. [f] In DCM with 0.1 M $[^nBu_4N]PF_6$ as the supporting electrolyte and Fc/Fc^+ as the internal reference (0.46 V *vs.* SCE).[29] The HOMO and LUMO energies were determined using $E_{HOMO/LUMO} = -(E_{ox}/E_{red} + 4.8)$ eV, where E_{ox} and E_{red} are anodic and cathodic peak potentials, respectively, obtained from the DPV *versus* Fc/Fc^+.[29] [g] $E_g = |E_{HOMO} - E_{LUMO}|$.

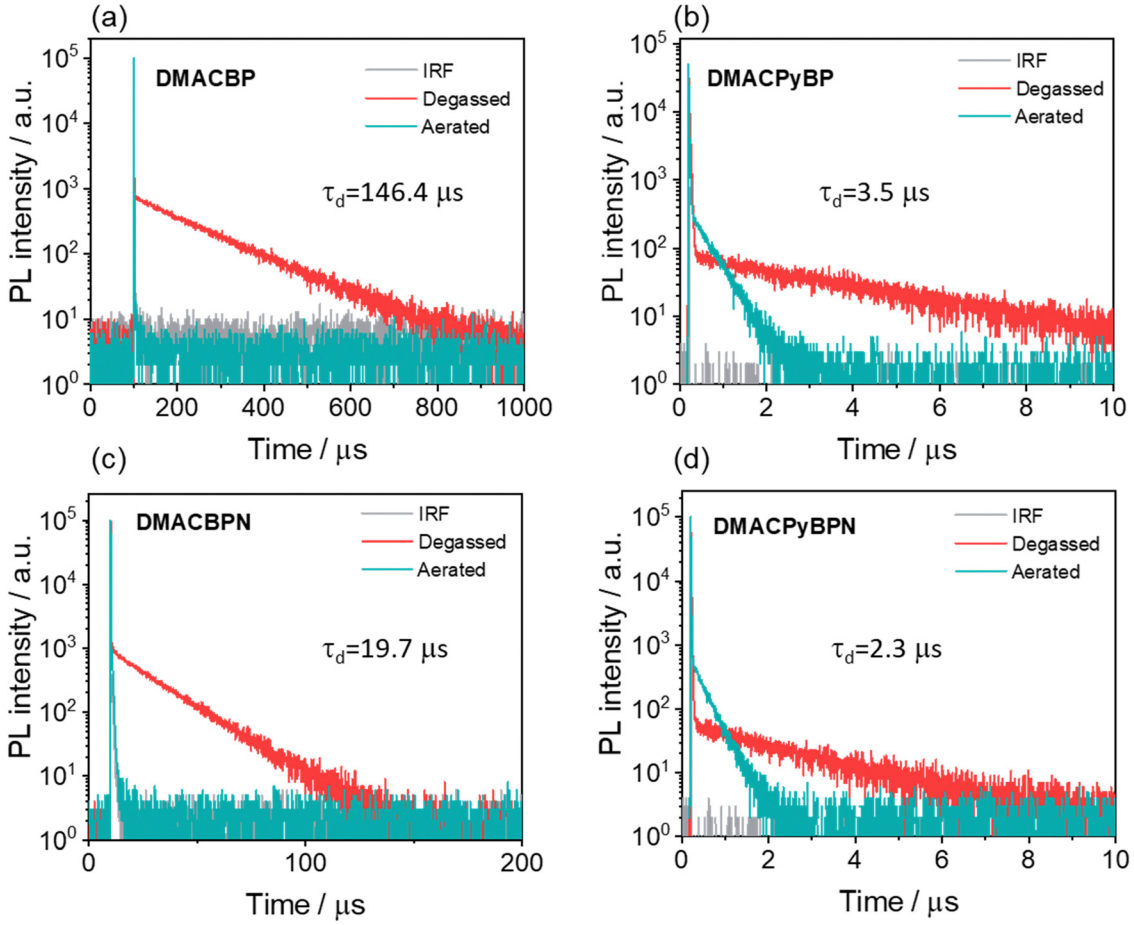

Fig. 4 Time-resolved PL decay of (a) **DMACBP**, (b) **DMACPyBP**, (c) **DMACBPN** and (d) **DMACPyBPN** in degassed and aerated toluene (time window: 1 ns to 200 μs or 1 ns to 1 ms measured by MCS, 1 ns to 10 μs measured by TCSPC, λ_{exc} = 375 nm).

DMACBP and **DMACBPN** is more significant than in **DMACPyBP** and **DMACPyBPN**, the latter two of which contain an additional pyridine ring fused to the pyrazine in the acceptor. The increased quenching of the PL of the former two compounds may be due to their longer delayed lifetimes. The emission intensity is likewise strongly affected by the presence of oxygen, especially for **DMACBP** and **DMACBPN**, while for **DMACPyBP** and **DMACPyBPN**, the enhancement in intensity upon oxygen removal was much smaller (Fig. S32, ESI‡). The PL decays with biexponential kinetics, with prompt fluorescence lifetimes, τ_p, of 18 ns, 21 ns, 27 ns and 10 ns (Fig. S33, ESI‡), and delayed fluorescence lifetimes, τ_d, of 146.4 μs, 3.5 μs, 19.7 μs and 2.3 μs, respectively, for **DMACBP**, **DMACPyBP**, **DMACBPN** and **DMACPyBPN**. The corresponding rate constants of intersystem crossing (k_{ISC}) for **DMACBP**, **DMACPyBP**, **DMACBPN** and **DMACPyBPN** are 4.1×10^7 s^{-1}, 3.3×10^7 s^{-1}, 2.9×10^7 s^{-1} and 5.0×10^7 s^{-1}, respectively, while the rate constants for reverse intersystem crossing (k_{RISC}) for **DMACPyBP** (81.6×10^4 s^{-1}) and **DMACPyBPN** (87.0×10^4 s^{-1}) are much faster than those of **DMACBP** (2.7×10^4 s^{-1}) and **DMACBPN** (24.1×10^4 s^{-1}), due in part to the smaller ΔE_{ST} in the former two that is correlated to the introduction of a nitrogen atom at the 10-position in **DMACPyBP** and **DMACPyBPN**.

We next investigated the photophysical properties of the four emitters in an OLED-relevant host, 4,4′-*N*,*N*′-dicarbazolebiphenyl (CBP), as this host matrix has sufficiently high triplet energy (T_1 = 2.56 eV) to confine the excitons onto the emitter.[35,36] The PL of the doped films of varying dopant concentrations from 2–10 wt% of emitters was first investigated (Fig. S36, ESI‡) and the corresponding Φ_{PL} values are summarized in Table S2 (ESI‡). As the doping concentration is increased, the emission of all of the compounds is red-shifted from yellow to red (Fig. S34, ESI‡), and the highest Φ_{PL} values are at a doping concentration of 2 wt%. The SSPL spectra of **DMACBP**, **DMACPyBP**, **DMACBPN** and **DMACPyBPN** at a doping concentration of 2 wt% exhibit broad and unstructured emission with λ_{PL} at 568, 601, 586, and 606 nm, respectively (Fig. 5(a)). The trend in λ_{PL} mirrors those in toluene (Fig. 3(b)). The Φ_{PL} values of these films of **DMACBP**, **DMACPyBP**, **DMACBPN** and **DMACPyBPN** are 75, 47, 71 and 37%, respectively, under a N_2 atmosphere (Fig. 5(b) and Table 1). The decrease in Φ_{PL} for **DMACPyBP**/**DMACPyBPN** can be ascribed to their smaller energy gaps, thus leading to increased non-radiative decay.[37] However, the difference in the distribution of N atoms in the BP and BPN (two additional nitrogen atoms on the 4- and 5-position) acceptors has only a relatively small impact on the acceptor strength,

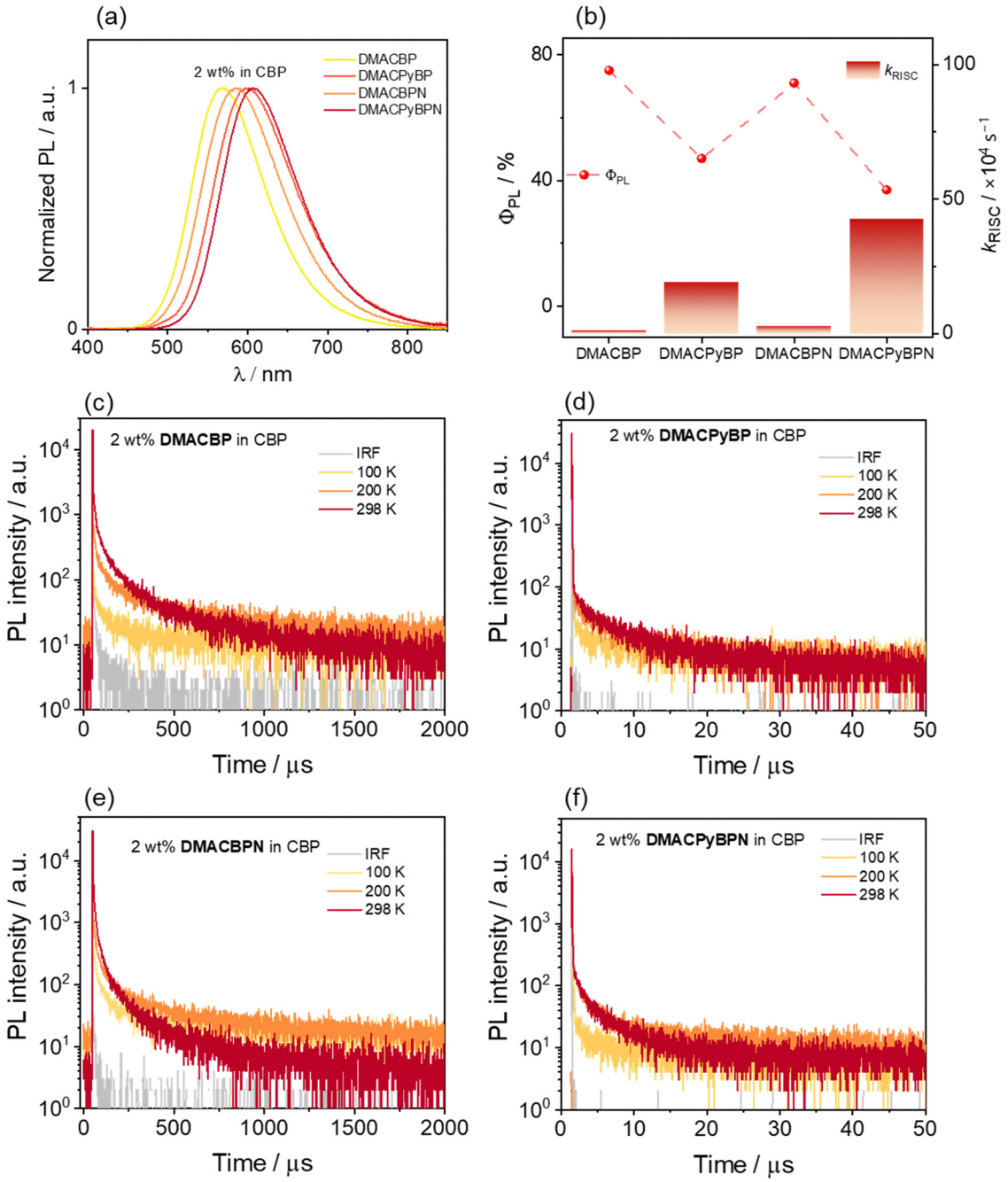

Fig. 5 (a) PL spectra of the **DMACBP**, **DMACPyBP**, **DMACBPN** and **DMACPyBPN** in 2 wt% doped films in CBP (λ_{exc} = 360 nm); (b) Φ_{PL} and k_{RISC} for each of the four emitters; temperature-dependent TRPL decays of (c) 2 wt% **DMACBP**, (d) 2 wt% **DMACPyBP**, (e) 2 wt% **DMACBPN** and (f) 2 wt% **DMACPyBPN** doped CBP films (λ_{exc} = 375 nm).

with a small red shift in the emission from 568 nm for **DMACBP** to 586 nm for **DMACBPN**; as well, there is only a negligible decrease in Φ_{PL} between **DMACBP** and **DMACBPN** (Table 1 and Fig. 5(b)).[38] The Φ_{PL} values of **DMACBP** and **DMACBPN** exhibited a larger decrease in the presence of air at 56 and 52%, respectively, compared to 41% for **DMACPyBP** and 30% for **DMACPyBPN**, indicating a greater proportion of triplet excitons in **DMACBP** and **DMACBPN**. As shown in Fig. 5, all four compounds showed multiexponential decay kinetics, with average prompt fluorescence lifetimes, average τ_p, of 15.3, 21.1, 22.4, and 23.2 ns (Fig. S35, ESI‡) and average delayed emission lifetimes, average τ_d, of 130.3, 5.9, 47.2, and 2.9 μs at room temperature for **DMACBP**, **DMACPyBP**, **DMACBPN** and **DMACPyBPN**, respectively. The corresponding k_{ISC} values for **DMACBP**, **DMACPyBP**, **DMACBPN** and **DMACPyBPN** in the 2 wt% doped films in CBP are 1.7×10^7 s^{-1}, 0.6×10^7 s^{-1}, 1.2×10^7 s^{-1} and 0.8×10^7 s^{-1}, respectively, while k_{RISC} for **DMACPyBP** and **DMACPyBPN** reached 1.94×10^5 s^{-1} and 4.26×10^5 s^{-1}, more than ten times

higher than those of **DMACBP** at 0.10×10^5 s^{-1} and **DMACBPN** at 0.29×10^5 s^{-1} (Fig. 5(b)), following a similar trend to that observed for toluene. The introduction of a nitrogen atom at the 10-position in **DMACPyBP** and **DMACPyBPN** leads to a much stronger CT and faster k_{RISC}. Temperature-dependent time-resolved PL (TRPL) analysis shows that the intensity of the delayed emission increases with increasing temperatures for all 4 compounds, confirming that these compounds emit *via* TADF (Fig. 5(c) and (d)). The energy levels of the S_1 and T_1 states were estimated from the onset of the corresponding prompt fluorescence and phosphorescence spectra of the 2 wt% doped films in CBP at 77 K (Fig. S36, ESI‡). As expected, **DMACBP**, **DMACPyBP**, **DMACBPN** and **DMACPyBPN** have, respectively, small ΔE_{ST} values of 0.02, 0.01, 0.01 and 0.01 eV, values consistent with those in 2-MeTHF glass.

Device characterization

To evaluate the electroluminescence (EL) performance of these emitters, OLEDs employing different doping concentration emitters (2, 5, 8 and 11 wt%, the data for 5 and 8 wt% can be found in Fig. S38 and Table S3, ESI‡) doped in CBP films as the emissive layer (EML) was fabricated. The OLEDs have the following configuration: ITO (indium tin oxide)/TAPC (4,4′-(cyclohexane-1,1-diyl)bis(*N*,*N*-di-*p*-tolylaniline)) (40 nm)/TCTA (tris(4-(9*H*-carbazol-9-yl)phenyl)amine) (10 nm)/CBP (10 nm)/CBP:*x* wt% dopants (20 nm)/TmPyPB (3,3′-(5′-(3-(pyridin-3-yl)phenyl)-[1,1′:3′,1″-terphenyl]-3,3″-diyl)dipyridine) (45 nm)/LiF (1 nm)/Al (Fig. 6(a)). ITO and Al serve as the anode and the cathode, respectively, while TAPC, TCTA and TmPyPB are, respectively, used as the hole-transporting layer, the electron-blocking layer, and the electron-transporting layer.

As shown in Fig. 6(b), the OLEDs with **DMACBP**, **DMACPyBP**, **DMACBPN** and **DMACPyBPN** at a doping concentration of 2 wt% in the CBP host exhibit yellow-to-red EL with the peak emission, λ_{EL}, at 576, 600, 588 and 608 nm, respectively, which match the PL in CBP very well (Fig. 5(a)). The corresponding CIE coordinates are (0.48, 0.50), (0.56, 0.44), (0.53, 0.46) and (0.57, 0.42). The devices with **DMACBP**, **DMACPyBP**, **DMACBPN**, and **DMACPyBPN** showed EQE_{max} of 18.5, 13.7, 19.4 and 10.5%, respectively, reflecting the variations in their intrinsic Φ_{PL} (Fig. 6(c) and Table 2). The maximum current efficiency (CE_{max}) and power efficiency (PE_{max}) values are 58.7 cd A^{-1} and 54.2 lm W^{-1} for the devices with **DMACBP**, 28.9 cd A^{-1} and 26.7 lm W^{-1} for the devices with **DMACPyBP**, 48.9 cd A^{-1} and 46.5 lm W^{-1} for the devices with **DMACBPN**, and 17.4 cd A^{-1} and 16.6 lm W^{-1} for the devices with **DMACPyBPN** (Fig. 6(d)), respectively. The efficiency roll-off behavior is noticeably different between the four devices. At a luminance of 100 cd m^{-2}, a large efficiency roll-off of 40.5% and 24.7% was observed in the devices with **DMACBP** and **DMACBPN**, respectively, which decreased considerably to 8.0% and 4.7% for the devices with **DMACPyBP** and **DMACPyBPN**, respectively. The EQE decreased to 3.7% at a luminance of 1000 cd m^{-2} for the device with **DMACBP**; however, for the device with **DMACPyBP**, the EQE_{1000} was 7.5%. Similarly, at the same current density of 1 mA cm^{-2}, the devices with **DMACBP** and **DMACBPN** exhibit much larger efficiency roll-off of 58% and 36%, respectively, than the devices with **DMACPyBP** (16%) and **DMACPyBPN** (14%)

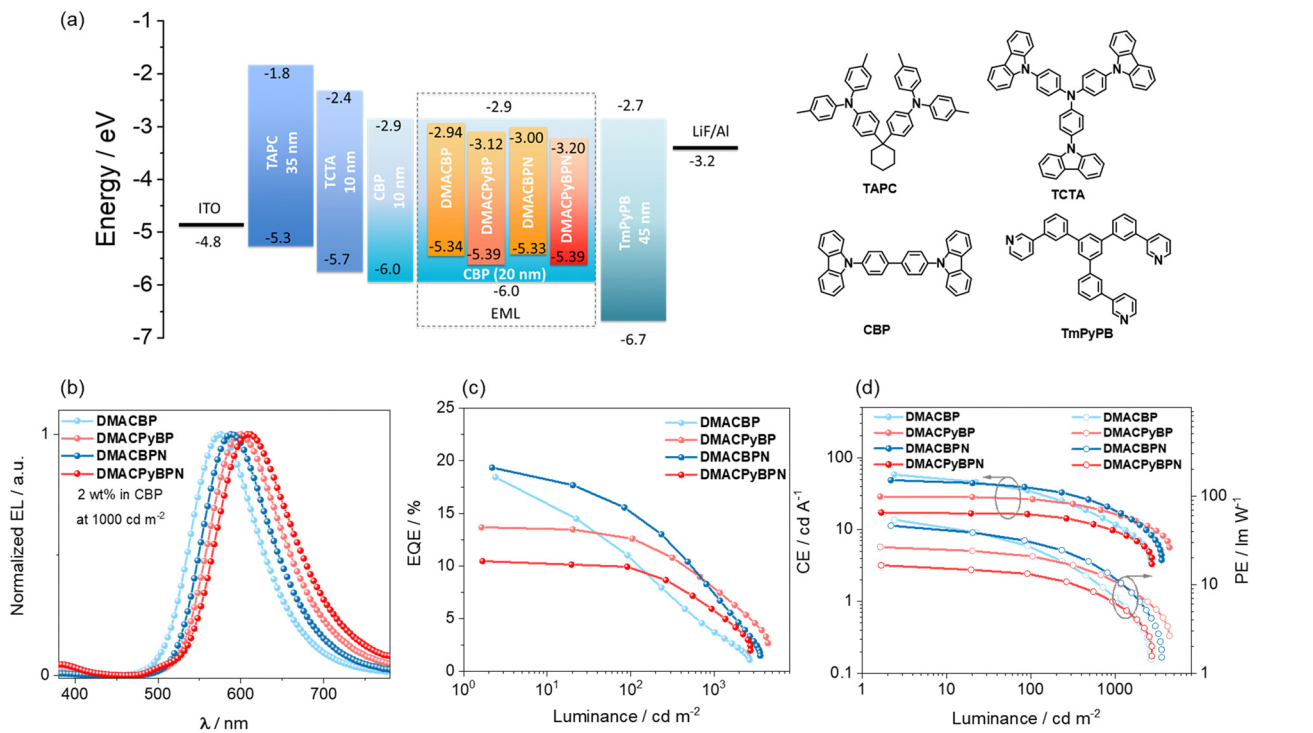

Fig. 6 (a) Energy level diagram and molecular structure of materials employed in the devices; (b) EL spectra of the devices; (c) external quantum efficiency *versus* luminance curves for the devices; (d) current efficiency and power efficiency *versus* luminance curves for the devices.

Table 2 Electroluminescence data for the devices

Emitter	Concentration/ wt%	V_{on}[a]/ V	CE_{max}[b]/cd A^{-1}	PE_{max}[c]/lm W^{-1}	$EQE_{max/100/1000}$[d]/ %	Efficiency roll-off $_{100/1000}$[e]/ %	L_{max}[f]/cd m^{-2}	λ_{EL}[g]/ nm	CIE[h] (x, y)
DMACBP	2.0%	3.4	58.7	54.2	18.5/11.0/3.7	40/80	2665	576	0.48, 0.50
	11.0%	3.5	38.1	34.2	14.6/12.0/5.6	18/62	4332	584	0.52, 0.47
DMACPyBP	2.0%	3.4	28.9	26.7	13.7/12.6/7.5	8/45	4346	600	0.56, 0.44
	11.0%	3.4	11.6	10.7	9.0/8.3/4.7	8/47	3369	620	0.61, 0.39
DMACBPN	2.0%	3.3	48.9	46.5	19.4/14.6/6.7	25/65	3551	588	0.53, 0.46
	11.0%	3.1	31.9	32.3	15.9/13.4/7.5	16/53	4315	600	0.57, 0.43
DMACPyBPN	2%	3.3	17.4	16.6	10.5/10.0/5.0	5/52	2723	608	0.57, 0.42
	11%	3.2	4.1	4.0	5.4/5.1/2.0	5/63	1428	640	0.63, 0.37

[a] Voltage at 1 cd m^{-2}. [b] Maximum current efficiency. [c] Maximum power efficiency. [d] Maximum external quantum efficiency at 100 cd m^{-2}/at 1000 cd m^{-2}. [e] EQE roll off at 100 cd m^{-2}/at 1000 cd m^{-2}. [f] Maximum luminance. [g] EL emission peak at 1000 cd m^{-2}. [h] Commission Internationale de L'Éclairage coordinates.

(as shown in Fig. S37, ESI‡). A plausible explanation for this difference in efficiency roll-off behavior is due to the faster k_{RISC} and shorter τ_d in **DMACPyBP** and **DMACPyBPN**, thus leading to smaller triplet exciton populations at high current densities in the devices with these two emitters. The **DMACPyBP**-based OLEDs showed remarkably low-efficiency roll-off, especially compared to other DMAC-containing orange-red TADF OLEDs (Fig. S1, ESI‡).[23,24,30] Increasing the doping concentration to 5 wt%, 8 wt% or even to 11 wt% does not lead to a further improvement in performance and the EL spectra red-shifted progressively (Fig. S38 and Table S3, ESI‡). At 11 wt% doping, the OLEDs emit in the range of 600–640 nm and showed an EQE_{max} of 5.5–15.9% (Table S3, ESI‡).

Conclusion

We have developed a family of four orange-to-red TADF compounds whose structures differ in the number of nitrogen atoms contained within the conjugated acceptor core. The structure–property relationship among the four compounds has been systematically investigated using DFT calculations and a combination of photophysical and electrochemical studies; OLEDs were also fabricated using these materials as emitters. It was found that increasing the nitrogen atom content in the acceptor (BP) of the D–A type compounds results in a more stabilized LUMO, a smaller ΔE_{ST} and a faster k_{RISC}. In particular, the presence of nitrogen at the 10-position of BP notably enhances k_{RISC}, as demonstrated in **DMACPyBP** and **DMACPyBPN** compared to **DMACBP** and **DMACBPN**, despite the small decrease in Φ_{PL}. OLEDs with **DMACBPN** showed a maximum EQE of 19.4% and an electroluminescence maximum of 588 nm. As the N/C ratio increased, the EL spectra of the corresponding devices progressively red-shifted, with the reddest-emitting device (λ_{EL} = 640 nm) employing **DMACPyBPN**. Furthermore, the **DMACPyBP**/**DMACPyBPN**-based OLEDs showed a remarkably low-efficiency roll-off of only 8 and 5%, compared to 40 and 25% at 100 cd m^{-2} for the devices with **DMACBP**/**DMACBPN**, respectively.

Conflicts of interest

There are no conflict to declare.

Acknowledgements

C. Si thanks the China Scholarship Council (201806890001). D. Sun acknowledges support from the Royal Academy of Engineering Enterprise Fellowship (EF2122-13106). The St Andrews team thanks EPSRC for financial support (EP/P010482/1). X.-H. Zhang acknowledges support from the National Natural Science Foundation of China (grant no. 52130304, 51821002), Suzhou Key Laboratory of Functional Nano & Soft Materials, Collaborative Innovation Center of Suzhou Nano Science & Technology, and the 111 Project.

References

1 D. Sun, C. Si, T. Wang and E. Zysman-Colman, *Adv. Photonics Res.*, 2022, 2200203.
2 M. Y. Wong and E. Zysman-Colman, *Adv. Mater.*, 2017, **29**, 1605444.
3 H. Uoyama, K. Goushi, K. Shizu, H. Nomura and C. Adachi, *Nature*, 2012, **492**, 234–238.
4 G. Hong, X. Gan, C. Leonhardt, Z. Zhang, J. Seibert, J. M. Busch and S. Bräse, *Adv. Mater.*, 2021, **33**, 2005630.
5 Y.-J. Yu, X.-Q. Wang, J.-F. Liu, Z.-Q. Jiang and L.-S. Liao, *iScience*, 2021, **24**, 102123.
6 Y. Liu, C. Li, Z. Ren, S. Yan and M. R. Bryce, *Nat. Rev. Mater.*, 2018, **3**, 18020.
7 J. H. Kim, J. H. Yun and J. Y. Lee, *Adv. Opt. Mater.*, 2018, **6**, 1800255.
8 Z. Yang, Z. Mao, Z. Xie, Y. Zhang, S. Liu, J. Zhao, J. Xu, Z. Chi and M. P. Aldred, *Chem. Soc. Rev.*, 2017, **46**, 915–1016.
9 Y. Xiao, H. Wang, Z. Xie, M. Shen, R. Huang, Y. Miao, G. Liu, T. Yu and W. Huang, *Chem. Sci.*, 2022, **13**, 8906–8923.
10 S. Sharma and A. K. Pal, *J. Mater. Chem. C*, 2022, **10**, 15681–15707.
11 J. S. Wilson, N. Chawdhury, M. R. A. Al-Mandhary, M. Younus, M. S. Khan, P. R. Raithby, A. Köhler and R. H. Friend, *J. Am. Chem. Soc.*, 2001, **123**, 9412–9417.
12 J. V. Caspar, E. M. Kober, B. P. Sullivan and T. J. Meyer, *J. Am. Chem. Soc.*, 1982, **104**, 630–632.
13 Y. J. Yu, Y. Hu, S. Y. Yang, W. Luo, Y. Yuan, C. C. Peng, J. F. Liu, A. Khan, Z. Q. Jiang and L. S. Liao, *Angew. Chem., Int. Ed.*, 2020, **59**, 21578–21584.

14 Y. Yuan, Y. Hu, Y. X. Zhang, J. D. Lin, Y. K. Wang, Z. Q. Jiang, L. S. Liao and S. T. Lee, *Adv. Funct. Mater.*, 2017, **27**, 1–5.
15 C. Li, R. Duan, B. Liang, G. Han, S. Wang, K. Ye, Y. Liu, Y. Yi and Y. Wang, *Angew. Chem., Int. Ed.*, 2017, **56**, 11525–11529.
16 R. Furue, K. Matsuo, Y. Ashikari, H. Ooka, N. Amanokura and T. Yasuda, *Adv. Opt. Mater.*, 2018, **6**, 1–9.
17 S. Wang, X. Yan, Z. Cheng, H. Zhang, Y. Liu and Y. Wang, *Angew. Chem., Int. Ed.*, 2015, **54**, 13068–13072.
18 S. Wang, Z. Cheng, X. Song, X. Yan, K. Ye, Y. Liu, G. Yang and Y. Wang, *ACS Appl. Mater. Interfaces*, 2017, **9**, 9892–9901.
19 Y. L. Zhang, Q. Ran, Q. Wang, Y. Liu, C. Hänisch, S. Reineke, J. Fan and L. S. Liao, *Adv. Mater.*, 2019, **31**, 1–7.
20 S. Kothavale, W. J. Chung and J. Y. Lee, *J. Mater. Chem. C*, 2020, **8**, 7059–7066.
21 S. Kothavale, W. J. Chung and J. Y. Lee, *J. Mater. Chem. C*, 2022, **10**, 6043–6049.
22 S. Kothavale, J. Lim and J. Yeob Lee, *Chem. Eng. J.*, 2022, **431**, 134216.
23 F. M. Xie, H. Z. Li, G. L. Dai, Y. Q. Li, T. Cheng, M. Xie, J. X. Tang and X. Zhao, *ACS Appl. Mater. Interfaces*, 2019, **11**, 26144–26151.
24 C. Zhou, W. C. Chen, H. Liu, X. Cao, N. Li, Y. Zhang, C. S. Lee and C. Yang, *J. Mater. Chem. C*, 2020, **8**, 9639–9645.
25 F. M. Xie, X. Y. Zeng, J. X. Zhou, Z. D. An, W. Wang, Y. Q. Li, X. H. Zhang and J. X. Tang, *J. Mater. Chem. C*, 2020, **8**, 15728–15734.
26 H. Wang, B. Zhao, P. Ma, Z. Li, X. Wang, C. Zhao, X. Fan, L. Tao, C. Duan, J. Zhang, C. Han, G. Chen and H. Xu, *J. Mater. Chem. C*, 2019, **7**, 7525–7530.
27 S. Hirata and M. Head-Gordon, *Chem. Phys. Lett.*, 1999, **314**, 291–299.
28 W. Humphrey, A. Dalke and K. Schulten, *J. Mol. Graphics*, 1996, **14**, 33–38.
29 N. G. Connelly and W. E. Geiger, *Chem. Rev.*, 1996, **96**, 877–910.
30 X. Y. Zeng, J. X. Zhou, S. J. Zou, Y. Q. Tang, H. Z. Li, Y. H. He, Y. Q. Li, W. J. Wang and J. X. Tang, *Adv. Opt. Mater.*, 2022, **10**, 1–9.
31 U. Balijapalli, Y. T. Lee, B. S. B. Karunathilaka, G. Tumen-Ulzii, M. Auffray, Y. Tsuchiya, H. Nakanotani and C. Adachi, *Angew. Chem., Int. Ed.*, 2021, **0395**, 19364–19373.
32 Y. U. Peter and M. Cardona, *Fundamentals of semiconductors: physics and materials properties*, Springer Science & Business Media, 2010.
33 T. C. Parker and S. R. Marder, *Synthetic methods in organic electronic and photonic materials: A practical guide*, Royal Society of Chemistry, 2015.
34 S. Karuthedath, J. Gorenflot, Y. Firdaus, N. Chaturvedi, C. S. P. De Castro, G. T. Harrison, J. I. Khan, A. Markina, A. H. Balawi, T. A. Dela Peña, W. Liu, R. Z. Liang, A. Sharma, S. H. K. Paleti, W. Zhang, Y. Lin, E. Alarousu, D. H. Anjum, P. M. Beaujuge, S. De Wolf, I. McCulloch, T. D. Anthopoulos, D. Baran, D. Andrienko and F. Laquai, *Nat. Mater.*, 2021, **20**, 378–384.
35 A. Endo and C. Adachi, *Chem. Phys. Lett.*, 2009, **483**, 224–226.
36 C. Adachi, R. C. Kwong, P. Djurovich, V. Adamovich, M. A. Baldo, M. E. Thompson and S. R. Forrest, *Appl. Phys. Lett.*, 2001, **79**, 2082–2084.
37 M. Albota, D. Beljonne, J. L. Brédas, J. E. Ehrlich, J. Y. Fu, A. A. Heikal, S. E. Hess, T. Kogej, M. D. Levin, S. R. Marder, D. McCord-Maughon, J. W. Perry, H. Röckel, M. Rumi, G. Subramaniam, W. W. Webb, X. L. Wu and C. Xu, *Science*, 1998, **281**, 1653–1656.
38 A. Hirono, H. Sakai, S. Kochi, T. Sato and T. Hasobe, *J. Phys. Chem. B*, 2020, **124**, 9921–9930.

